


Cluster glass behavior of the frustrated birnessites $A_x\text{MnO}_2 \cdot y\text{H}_2\text{O}$ ($A = \text{Na}, \text{K}$)

L. D. Kulish ^{*}, R. Scholtens, and G. R. Blake*Zernike Institute for Advanced Materials, University of Groningen, Nijenborgh 4, 9747 AG, Groningen, the Netherlands*

(Received 1 October 2019; revised manuscript received 5 November 2019; published 26 December 2019)

We report the synthesis and magnetic properties of frustrated $\text{Na}_{0.22}\text{MnO}_2 \cdot 0.39\text{H}_2\text{O}$ and $\text{K}_{0.6}\text{MnO}_2 \cdot 0.48\text{H}_2\text{O}$ with the birnessite structure. The structure, static, and dynamic magnetic properties of the compounds are investigated in detail. A combination of DC and AC magnetic susceptibility measurements and magnetization decay measurements reveal cluster glass behavior below the freezing temperature of 4 K for Na-birnessite and 6 K for K-birnessite. The frequency dependence of the freezing temperature is analyzed on the basis of dynamic scaling laws including the critical slowing-down formula and the Vogel-Fulcher law, which further confirm cluster glass formation in both compounds.

DOI: [10.1103/PhysRevB.100.214435](https://doi.org/10.1103/PhysRevB.100.214435)

I. INTRODUCTION

Magnetically frustrated compounds are promising for the emergence of various exotic magnetic states. For example, they can exhibit spin-liquid and spin-ice behavior, act as valence-bond solids, or exhibit an array of helical and cycloidal spirals or even a variety of periodic states with non-trivial topologies composed of skyrmions and antiskyrmions [1–3]. Magnetic frustration often results from competition between ferromagnetic (FM) and antiferromagnetic (AFM) exchange interactions in crystal lattices based on triangles or tetrahedra that share corners, edges, or faces [4,5].

One group of interesting compounds from this point of view is the alkali manganites $A_x\text{MnO}_2 \cdot y\text{H}_2\text{O}$ ($A = \text{Na}, \text{K}$) with the birnessite structure (hereafter referred to as Na/K-bir). These antiferromagnetic compounds have frustrated two-dimensional triangular planes of magnetic $\text{Mn}^{3+/4+}$ ions, which form edge-shared MnO_6 octahedral structural units. The planes are separated from each other by gaps containing nonmagnetic A^+ cations and H_2O molecules [6]. This type of structure, with weakly coupled planes of spins pointing typically in the out-of-plane direction, allows tuning of the interlayer distance, the ratio of $\text{Mn}^{3+}/\text{Mn}^{4+}$, and thus the magnetic exchange and anisotropy along the stacking direction.

The exact crystal structure of birnessites remains unclear in terms of the placement of the interlayer species and the presence of Mn vacancies [7,8]. Due to high ionic mobility, it is difficult to determine whether the alkali cations and water molecules occupy the same or different positions in the interlayer space. At the same time, this high mobility of the interlayer cations has led to the wide use of birnessite compounds in the field of battery storage as capacitors showing high cycling capability [9–11]. Furthermore, birnessite compounds have been demonstrated as molecular sieves for purposes such as water purification [12]. Concerning vacan-

cies in the manganese layers, it has been suggested that their existence probably depends on synthesis conditions [8].

Relatively few studies have been reported on the magnetic properties of birnessite compounds. Birnessitelike MnO_2 nanowalls exhibited antiferromagnetic behavior with an ordering transition at 9.2 K and a bifurcation of the zero-field-cooled and field-cooled DC susceptibilities [13]. No information is available on K-containing birnessites and only one study has been performed on water-containing Na-birnessite structures, namely for $\text{Na}_{0.36}\text{MnO}_2 \cdot 0.2\text{H}_2\text{O}$ [14]. This might be due to the difficulty in synthesizing phase-pure birnessite samples; powder x-ray diffraction (XRD) on the samples studied in Ref. [14] revealed impurities of α - and β - NaMnO_2 , and possibly Mn_3O_4 , all of which are magnetic phases. It was shown that a spin-glass state is present below 29 K and it was speculated that there is a random static distribution of $\text{Mn}^{3+}/\text{Mn}^{4+}$ cations in the matrix of the birnessite compound. However, the influence of the impurity phases on the magnetic data in this study was not discussed.

For a better understanding of the nature of birnessite compounds, it should also be mentioned that a closely related type of layered manganese oxides is known—the α and β - NaMnO_2 phases without crystal water in the interlayer space. These compounds have been well investigated in terms of their electrical and magnetic properties. Because they contain Mn^{3+} —a strongly Jahn-Teller active cation, the MnO_6 octahedra are distorted along the $[-1\ 0\ 1]$ crystallographic direction. The α - NaMnO_2 [15,16] phase adopts the monoclinic $C2/m$ space group and consists of flat sheets of edge-shared MnO_6 octahedra separated by Na^+ ions, similar to Na-bir. Another similarity is the possibility of Na vacancies in the structure which would also lead to mixed-valent manganese ions, but in the birnessite structure the Na/Mn molar ratio is less than 0.7 whereas for α - NaMnO_2 , the ratio is >0.7 . The β - NaMnO_2 [17] phase differs from the α phase in that the MnO_6 octahedra form zigzag sheets separated by Na atoms; the space group is orthorhombic $Pmnm$ [18].

The α -phase polymorph $\text{Na}_{0.9}\text{MnO}_2$ has unfrustrated nearest-neighbor manganese atoms with a dominant AFM exchange interaction along the short b axis and frustrated

^{*}l.kulish@rug.nl

next-nearest-neighbor AFM exchange due to four equivalent exchange pathways. This frustrated interchain coupling leads to quasi-one-dimensional magnetic interactions [19] in this compound at temperatures as high as 200 K. Below the Néel temperature of 45 K, the triangular lattice hosts the coexistence of a short-range incommensurately modulated AFM state with a short-range commensurate AFM state which becomes dominant below 22 K. The presence of a small amount of Mn^{4+} cations is manifested as a random, static magnetic impurity within the MnO_6 planes [15].

In the case of β - NaMnO_2 , it was shown that a spontaneous long-range collinear AFM order appears below 200 K. Moreover, a transition to a spatially modulated proper screw magnetic state was found at 95 K. Between these two transitions a magnetically inhomogeneous state exists, and a spin gap (~ 5 meV) opens in the low-temperature state [20].

Summarizing current knowledge of these systems, a precise description of the magnetic properties of birnessite compounds remains obscure, specifically, the influence of the mixed oxidation state of the manganese ions, the distribution of $\text{Mn}^{3+/4+}$ in the matrix, as well as how the alkali cation deficiency and the number of water molecules can be controlled to tune the magnetic properties. Here we take steps to explore the structure and magnetic behavior of birnessite compounds. We utilize sol-gel synthesis to obtain pure samples of the birnessite compounds $A_x\text{MnO}_2 \cdot y\text{H}_2\text{O}$ ($A = \text{Na}, \text{K}$). Powder XRD shows that the $\text{Mn}^{3+}/\text{Mn}^{4+}$ cations are randomly distributed within the MnO_6 layers. Na-bir has a monoclinic structure with space group $C2/m$, whereas K-bir is triclinic with space group $C\bar{1}$. We use DC and AC magnetic susceptibility studies together with magnetization decay measurements to show that both systems have a glassy nature below their freezing temperatures. The frequency dispersion of the temperature-dependent AC susceptibility can be described by dynamic scaling theory and the Vogel-Fulcher law, which identify these systems as cluster glasses.

II. EXPERIMENTAL DETAILS

Bulk Na/K-bir samples were prepared by a sol-gel process earlier described by Ching *et al* [21]. First, TEAMnO_4 (TEA = tetraethylammonium) was synthesized by adding tetraethyl-ammonium bromide (TEABr) to KMnO_4 (1:1 molar ratio) in water [22]. The solution was stirred for 24 h, after which the precipitate of TEAMnO_4 was collected and dried under vacuum at room temperature to avoid thermal degradation. The typical yield of the reaction was 40% due to the partial water solubility of the salt. Next, 0.4 g (1.1 mmol) of TEAMnO_4 was added to 6 ml of a 0.9-M Na/K acetate in methanol solution. The solution slowly turned from purple to red and eventually to brown after ~ 1.5 h at room temperature. The color change results from the reduction of the Mn^{7+} ion to

$\text{Mn}^{4+}/\text{Mn}^{3+}$, which is paired with the oxidation of methanol. During this process the sol forms a gel. Excess methanol was then decanted and the gel was dried at 110°C for 24 h forming a xerogel. The xerogel was calcined at 450°C for 2 h to yield a dark-brown powder. After the powder was washed with water (3 times for K-bir and 20 times for Na-bir due to its less-hygroscopic nature), it was dried at 50°C .

Various characterization methods were used to probe the formation of Na/K-bir and to give information on the structural and magnetic properties. The phase purity and the crystal structure of the products were determined by x-ray diffraction. Powder XRD was carried out on a Bruker D8 Advance diffractometer operating with $\text{Cu K}\alpha$ radiation. Measurements were performed in the 2θ range 10 – 80° . The XRD data were fitted by Rietveld refinement using the GSAS software. To establish the particle shape and the size of birnessite compounds, scanning electron microscopy (SEM, FEI Helios G4 CX DualBeam) was performed. The dehydration processes on heating were investigated by means of simultaneous thermogravimetric analysis (TG) and differential scanning calorimetry (DSC) on a TG 2960 SDT instrument using an argon flow of 100 mL/min; the heating rate was $10^\circ\text{C}/\text{min}$ over the temperature range 30 to 500°C . Magnetic measurements were performed on a Quantum Design MPMS superconducting quantum interference device-based magnetometer. Magnetic susceptibility scans were performed on warming over the range 2–200 K, and magnetization versus applied field curves were obtained between -7 and 7 T at 2.5 K for Na-bir and 5 K for K-bir. AC susceptibility measurements were performed using a 3.8-Oe oscillating field superimposed on a 200-Oe DC field. Magnetization decay experiments were performed by applying a 1-T field, cooling the sample to 25 K at 1 K/min, holding for 10 min, and then cooled at 1 K/min to 2.5 K for Na-bir and 5 K for K-bir (below the glass freezing temperature). After 1 min, the field was removed and the magnetization was measured as a function of time.

III. RESULTS AND DISCUSSION

A. Structural characterization

The chemical compositions of the compounds were determined by a combination of simultaneous thermal analysis (TG and DSC) and a back-titration method (details are given in Appendix A). The calculated amount of water and average manganese oxidation state (+3.78 for Na-bir and +3.37 for K-bir assuming no oxygen or manganese vacancies) yield stoichiometries of $\text{Na}_{0.22}\text{MnO}_2 \cdot 0.39\text{H}_2\text{O}$ and $\text{K}_{0.6}\text{MnO}_2 \cdot 0.48\text{H}_2\text{O}$.

Structural analysis of our Na/K-bir samples using powder XRD shows single-phase products in both cases. The 001 peaks at $2\theta \approx 12.5^\circ$ are consistent with the ~ 7 -Å interlayer spacing expected for the birnessite compounds [14,23]. The

TABLE I. Compositions and structural parameters of Na/K-bir samples.

Compound	Space group	a	b	c	α	β	γ	Volume
$\text{Na}_{0.22}\text{MnO}_2 \cdot 0.39\text{H}_2\text{O}$	$C2/m$	4.923(1)	2.857(1)	7.277(2)	90	102.01(2)	90	100.09 (4)
$\text{K}_{0.6}\text{MnO}_2 \cdot 0.48\text{H}_2\text{O}$	$C\bar{1}$	5.006(2)	2.878(1)	7.281(2)	88.84(3)	101.21(3)	89.33 (4)	102.89 (5)

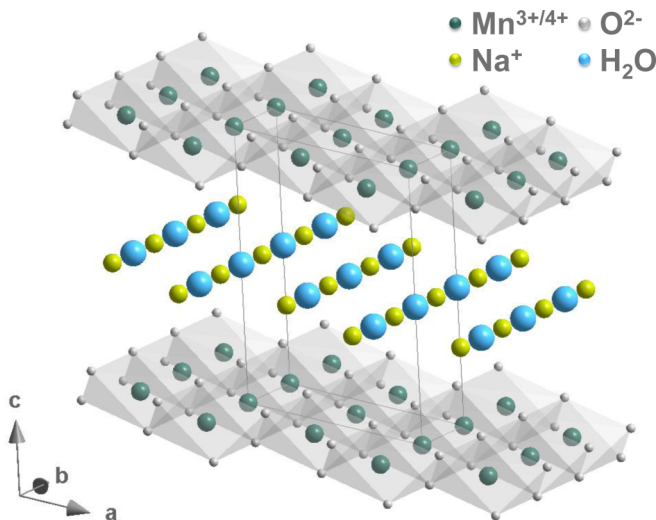


FIG. 1. Schematic representation of the crystal structure of $\text{Na}_{0.22}\text{MnO}_2 \cdot 0.39\text{H}_2\text{O}$. The manganese, oxygen, and sodium atoms are represented by dark green, gray, and green-yellow spheres respectively; the H_2O molecules are represented by the blue spheres. One unit cell is indicated by the dark gray lines.

space group is monoclinic $C2/m$ for Na-bir and triclinic $C\bar{1}$ for K-bir. The refined lattice parameters are listed in Table I, and details of the XRD analysis are given in Appendix B. In both structures, manganese cations occupy a single crystallographic position, which implies randomly distributed $\text{Mn}^{3+}/\text{Mn}^{4+}$ cations within the MnO_6 layers (Fig. 1).

The SEM images in Fig. 2 show that the sol-gel process led to the formation of irregular agglomerates of flat, round particles with different sizes. In the case of K-bir the particle sizes range from 25 to 100 nm, where the Na-bir particles are bigger with sizes from 45 to more than 200 nm.

B. DC magnetic susceptibility

The magnetic properties of Na/K-bir were initially investigated by performing DC magnetization measurements. Zero-field-cooled (ZFC) and field-cooled (FC) measurements

were performed in an applied magnetic field of 500 Oe on warming over the temperature range 2–200 K. A dependence on the thermal-magnetic history of the samples was observed, namely a bifurcation of the FC and ZFC curves below a characteristic temperature T_{irr} [Fig. 3(a)]. Such splitting can arise from a variety of phenomena such as spin glass/cluster glass (SG/CG), spin liquid, superparamagnetic, disordered antiferromagnetic and spin-spiral states [24]. The FC magnetization shows a continuous increase upon lowering the temperature. Simultaneously, the ZFC curve displays a well-defined peak at a temperature $T_g = 3.5$ K for Na-bir and 6.5 K for K-bir (Table II). The position of T_g is slightly below T_{irr} for both compounds. This behavior can be a manifestation of magnetic clusters, because for a canonical SG it generally holds that $T_{\text{irr}} \lesssim T_g$ [25,26].

The inverse susceptibility of the samples [Fig. 3(b)] is linear above 50 K; at lower temperature it starts to deviate, most likely due to short-range interactions. The extracted negative Curie-Weiss temperature θ_{CW} (Table II) suggests that the interactions are antiferromagnetic in both cases. The effective moment μ_{eff} is $3.76 \mu_B$ for Na-bir and $3.40 \mu_B$ for K-bir. The theoretical spin-only μ_{eff} for Mn^{4+} is $3.88 \mu_B$; μ_{eff} is $2.83 \mu_B$ for the Mn^{3+} low-spin state and $4.9 \mu_B$ for the Mn^{3+} high-spin state [24]. Our measured values imply that the Mn cations adopt a mixed-valent configuration of Mn^{4+} and low-spin Mn^{3+} . Since the presence of Mn^{4+} can suppress the Jahn-Teller distortion associated with Mn^{3+} under octahedral crystal fields, the low-spin state can become favored [27]. This configuration yields average oxidation states calculated from μ_{eff} of $\text{Mn}^{3.7+}$ for Na-bir and $\text{Mn}^{3.35+}$ for K-bir, which are in good agreement with the corresponding average oxidation states obtained by the back-titration method of $\text{Mn}^{3.78+}$ and $\text{Mn}^{3.37+}$, respectively. We note that a previous study of $\text{Na}_{0.36}\text{MnO}_2 \cdot 0.2\text{H}_2\text{O}$ also identified a low-spin Mn^{3+} state [14].

The presence of magnetic frustration can be inferred from the frustration parameter f , which is the ratio of $|\theta_{\text{CW}}|$ to the magnetic ordering temperature. However, this parameter is only valid if a long-range-ordered state is reached at some temperature, which does not seem to be the case above 2 K (the limit of our measurements) for Na/K-bir. The frustration

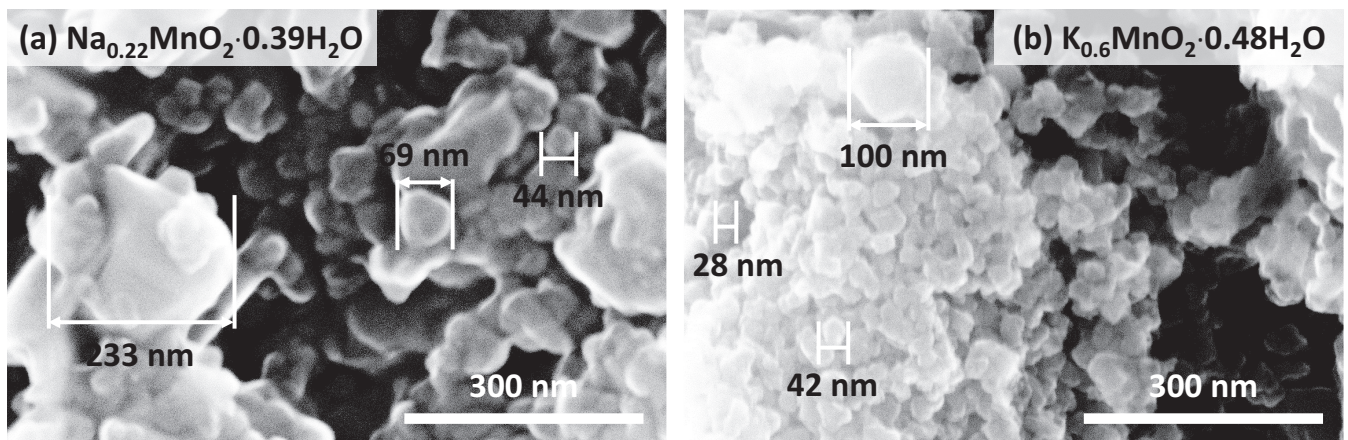


FIG. 2. SEM images of (a) Na-birnessite, (b) K-birnessite.

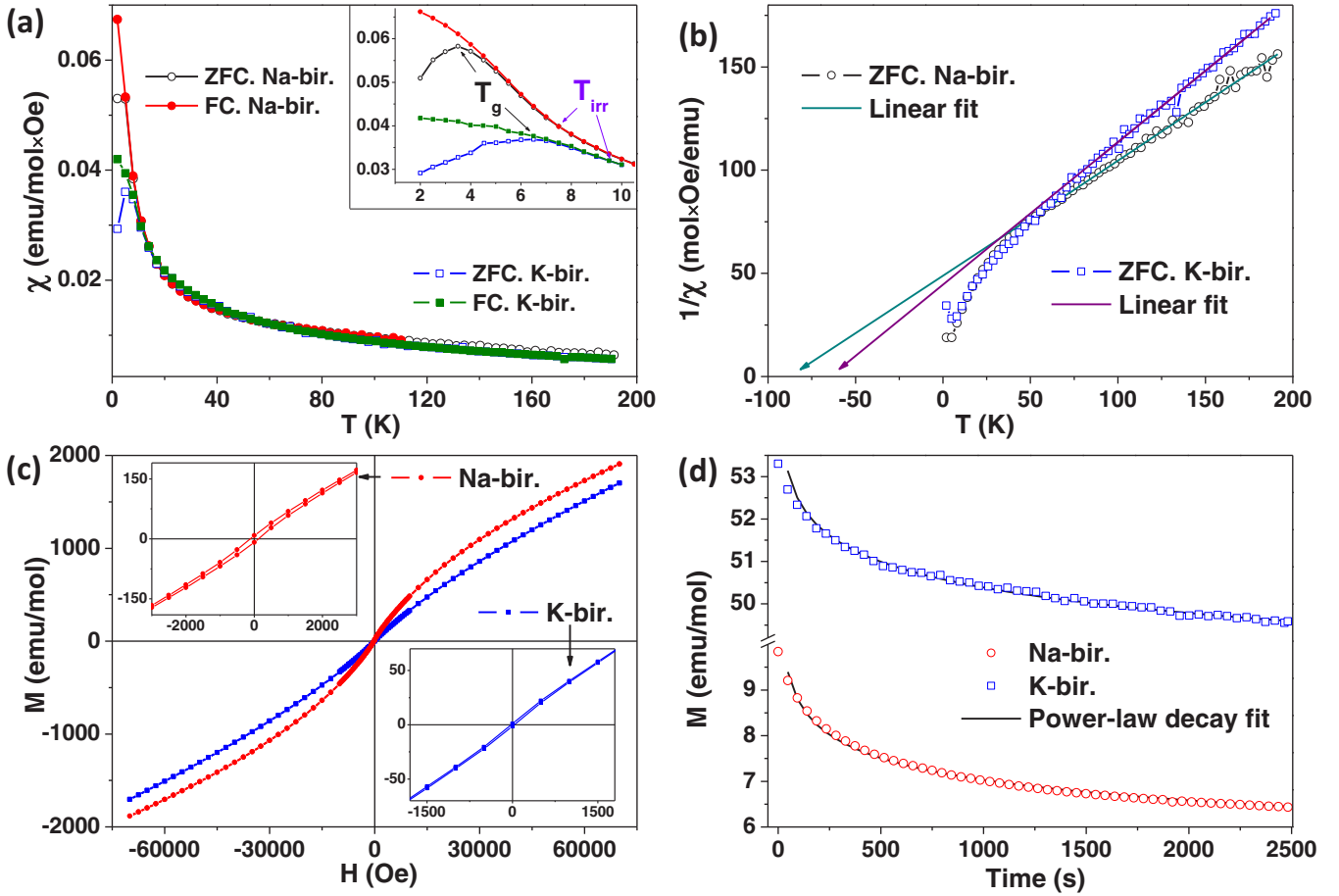


FIG. 3. (a) Temperature dependence of ZFC (open symbols) and FC (solid symbols) DC magnetic susceptibility of Na-bir (black and red) and K-bir (blue and green) measured on warming in a field of 500 Oe. The inset shows the DC susceptibility of samples in the 2–10 K range. (b) ZFC inverse DC susceptibility of Na-bir (black open symbols) and K-bir (blue open symbols) as a function of temperature at 500 Oe. The lines are linear fits to the experimental data above 50 K using the Curie-Weiss law. (c) Magnetization vs applied DC field measurement at 2.5 K for Na-bir (red) and at 5 K for K-bir (blue). The insets show closer views of the low-field region. (d) Magnetization decay measured by cooling Na-bir (red) and K-bir (blue) under a 1-T field to 2.5 K for Na-bir and 5 K for K-bir, then removing the field and measuring the magnetization as a function of time. The curves are fits to the experimental data using the power-law decay formula [Eq. (2)].

parameter can be approximated as $f = |\theta_{CW}|/T_g$ [5]. For both our compounds, $|\theta_{CW}|$ is ten or more times greater than T_g , implying a high level of frustration (Table II).

C. AC susceptibility

To further investigate the origin of the peaks observed in the ZFC curves [Fig. 3(a)], the temperature dependence of the AC susceptibility χ_{AC} was measured over the temperature range 2–12 K at six different frequencies: 1, 10, 50, 100, 500, 1000 Hz for Na-bir and 50, 100, 250, 500, 750, 1000 Hz for K-bir; measurements at frequencies of 1 and 10 Hz for K-bir were too noisy for reliable results to be extracted. AC

susceptibility measurements [28,29] are an important tool in the characterization of phase transitions and magnetic dynamics such as spin-glass freezing, antiferromagnetic-paramagnetic transitions, and various magnetic relaxation processes including the irreversible movement of domain walls, narrow hysteresis loops in ferromagnets, spin-lattice relaxation in paramagnets, and relaxation of superparamagnets [30–34].

The obtained AC-data (Fig. 4) consist of real and imaginary parts. The real component $\chi'(T)$ is in phase with the oscillating field and probes reversible magnetization processes [30]. The $\chi'(T)$ curves of both samples exhibit a maximum that both decreases in height and shifts to higher temper-

TABLE II. Summary of magnetic parameters of Na/K-bir.

Compound	T_g (K)	T_{irr} (K)	θ_{CW} (K)	μ_{eff} (μ_B)	δ	M_0 (emu/mol)	α
$\text{Na}_{0.22}\text{MnO}_2 \cdot 0.39\text{H}_2\text{O}$	3.5	7.5	−85	3.76	0.015	1.85×10^{-5}	9.5×10^{-2}
$\text{K}_{0.6}\text{MnO}_2 \cdot 0.48\text{H}_2\text{O}$	6.5	9.5	−63	3.40	0.027	4.98×10^{-5}	1.7×10^{-2}

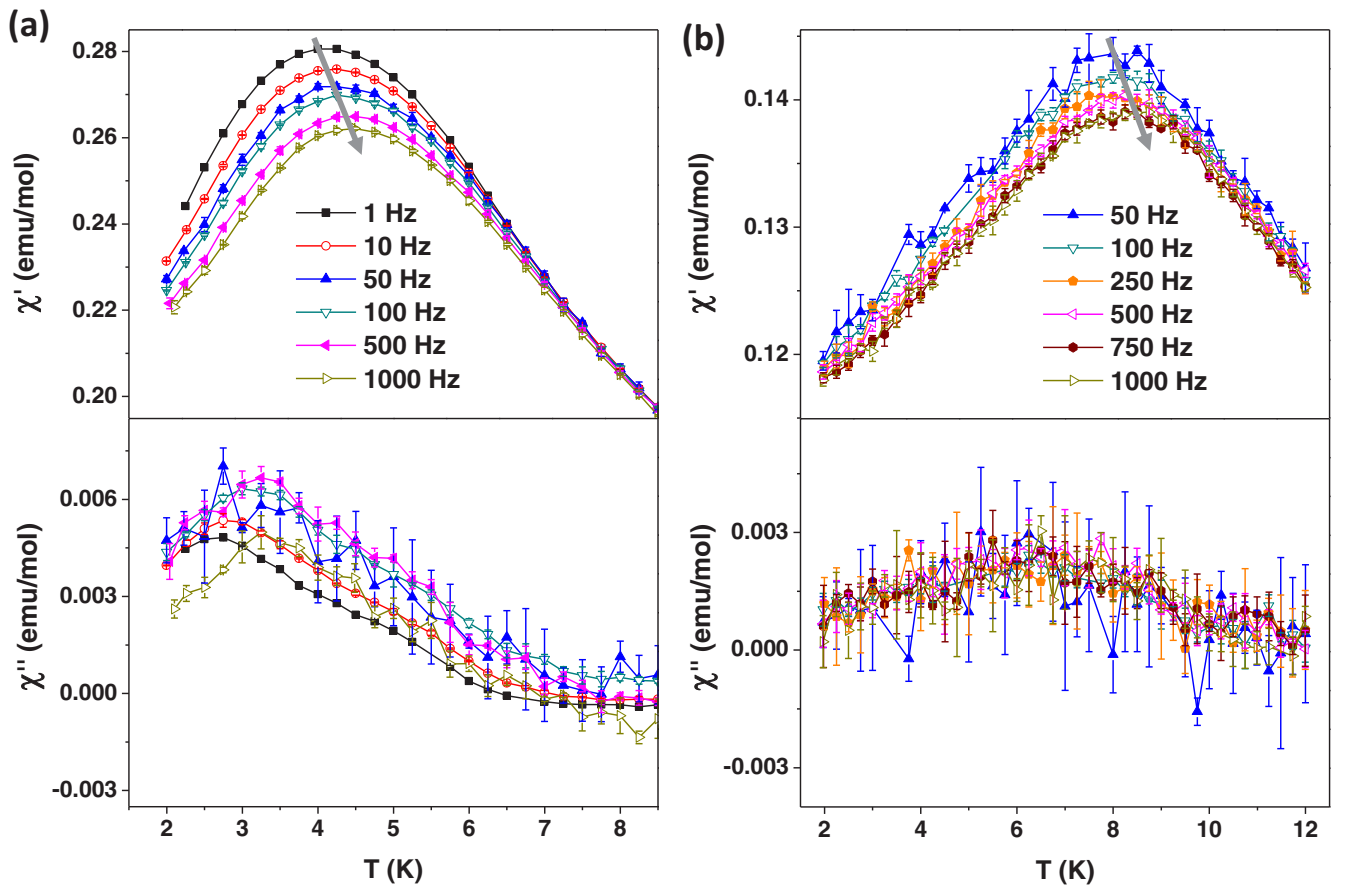


FIG. 4. Temperature dependence of the real and imaginary parts of the AC susceptibility at different frequencies, measured using a 3.8-Oe oscillating field and a 200-Oe DC field: (a) Na-birnessite at 1, 10, 50, 100, 500, 1000 Hz in the temperature range 2–9 K; (b) K-birnessite at 50, 100, 250, 500, 750, 1000 Hz in the temperature range 2–12 K.

ature with increasing frequency; in the case of Na-bir this shift is more pronounced. The temperature of this maximum, which we refer to as T_f , is in both cases between 0.5 and 1.5 K higher (depending on frequency) than T_g , at which the peak in the ZFC DC susceptibility is observed. Moreover, T_f approximately corresponds to the temperature at which the inflection point is observed in the imaginary part $\chi''(T)$ [25,31,35]. The imaginary component represents losses due to irreversible magnetization processes, which can involve different relaxations and energy absorbed from the applied field [30]. The maximum in $\chi''(T)$ shifts to higher temperature with frequency in the case of Na-bir, but there is little or no shift for K-bir. At temperatures above T_f , $\chi''(T)$ tends toward zero. Such behavior is characteristic for a SG transition [36,37].

A quantitative measure of the frequency dependence of the maximum in $\chi'(T)$ is given by the Mydosh parameter δ [34]:

$$\delta = \frac{\Delta T_f}{T_f \times \Delta[\ln(\omega)]}. \quad (1)$$

Here T_f is the freezing temperature, the frequency is $\omega = 2\pi f$, and ΔT_f is the difference between the maximum and minimum values of T_f . The Mydosh parameter allows magnetic states such as a SG [34] ($0.005 < \delta < 0.06$) and a noninteracting ideal superparamagnet ($\delta \leq 0.1$) to be distinguished [38,39]. The values of δ for Na/K-bir (Table II) correspond

to the intermediate situation of a CG, also referred to as a reentrant spin glass, for which $\delta \sim 0.01$ – 0.09 [25,26,40–43]. This suggests that the maximum in $\chi'(T)$ is associated with randomly arranged, interacting magnetic clusters which become frozen below T_f . We note that a smaller value of $\delta = 0.007$ was obtained in the previous study of $\text{Na}_{0.36}\text{MnO}_2 \cdot 0.2\text{H}_2\text{O}$ by Bakaimi *et al.* [14], corresponding to the canonical spin-glass regime.

D. Magnetization versus applied field

The presence of spin clusters should be reflected in the shape of the magnetization (M) versus applied field (H) curve. The M - H curves measured below T_f (at 2.5 K for Na-bir and 5 K for K-bir) exhibit an “S” shape in both cases [Fig. 3(c)], which taken alongside other evidence can also be a sign of spin-glass/cluster glass systems in the frozen state, as was shown for other glassy compounds [11,26,36,42]. The magnetization does not reach saturation up to the highest applied field of 7 T (the expected saturation magnetization is 1.80×10^4 emu/mol for Na-bir and 2.01×10^4 emu/mol for K-bir). For Na-bir there is a narrow hysteresis loop but for K-bir any hysteresis is smaller than the step size in H [see insets in Fig. 3(c)]. The existence of the hysteresis loop for Na-bir excludes a superparamagnetic ground state [44] and can be explained by the presence of competing

FM and AFM exchange interactions in the glassy state [11]. The ferromagnetic interactions might arise from neighboring Mn^{4+} cations, which in the triangular lattice of edge-sharing octahedra in the birnessite structure have $\text{Mn}^{4+}\text{-O-Mn}^{4+}$ bond angles of between 106 and 110° (see Table IV), favoring FM superexchange [45]. Ferromagnetic double exchange is unlikely here due to the low-spin state of Mn^{3+} . Na-bir has a larger FM contribution, which is consistent with the higher average oxidation state of $\text{Mn}^{3.78+}$ compared to $\text{Mn}^{3.37+}$ for K-bir.

E. Magnetization decay

To investigate the mechanism by which the system decays back to equilibrium after an external magnetic field is applied, magnetization decay measurements were carried out on both compounds [Fig. 3(d)]. The measured data follow a power-law decay and can be fitted by the equation [46]

$$M(t) = M_0 \times t^{-\alpha}. \quad (2)$$

Here M_0 is the maximum magnetization at the start of the measurement, and α is the decay parameter which is correlated with the decay rate. A higher decay parameter results

in faster decay. This model can be applied to describe SG systems [47], for which typical decay parameters [46] are on the order of 10^{-2} . The fitted curves match the data well, with extracted parameters of $M_0 = 1.85 \times 10^{-5}$ emu/mol, $\alpha = 9.5 \times 10^{-2}$ for Na-bir, and $M_0 = 4.98 \times 10^{-5}$ emu/mol, $\alpha = 1.7 \times 10^{-2}$ for K-bir. Thus, the magnetization of K-bir decays significantly more slowly. These decay parameters imply relatively long timescales, and are consistent with glassy behavior [34].

F. Dynamic scaling

To better understand the nature of the glassy phase of Na/K-bir, the dynamics of the SG state was studied by further analysis of the AC susceptibility measurements in Fig. 4. The frequency dependence of $\chi'(T)$ can be described by the critical slowing-down formula [48] from dynamic scaling theory:

$$\tau = \tau_0 \times \left[\frac{T_f - T_g}{T_g} \right]^{-z\nu}. \quad (3)$$

Here T_f was taken from the peak in $\chi'(T)$ for a given frequency f , and T_g is the temperature at which the maximum

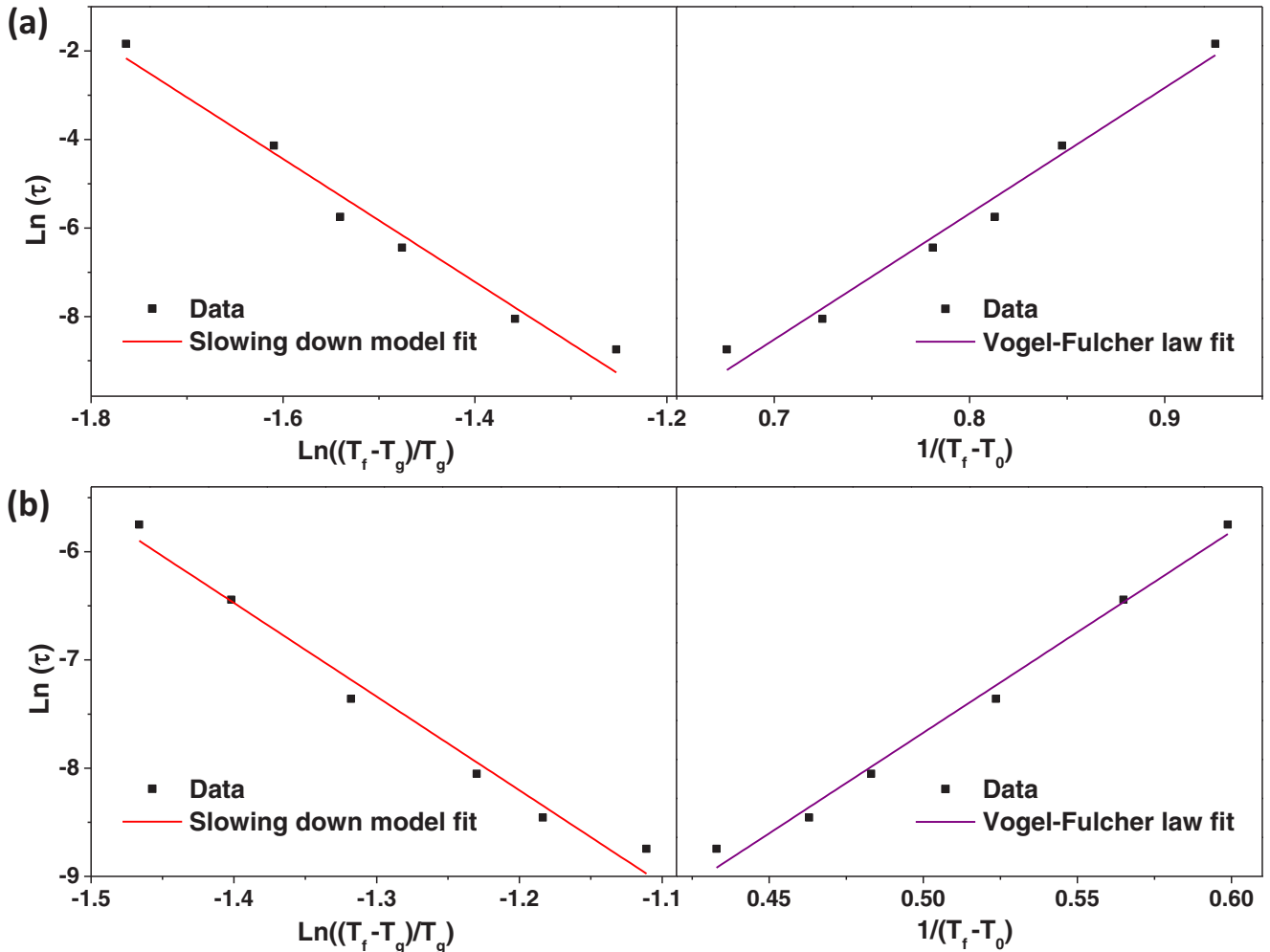


FIG. 5. Fits to AC susceptibility data ([temperature at which peak in $\chi'(T)$ occurs for different frequencies] using the slowing-down formula [Eq. (3)] and the Vogel-Fulcher law [Eq. (4)] for (a) Na-birnessite, (b) K-birnessite.

in the ZFC DC susceptibility is observed, because T_g can be regarded as the value of T_f for infinitely slow cooling ($\lim_{f \rightarrow 0} T_f$) [26]. The characteristic relaxation time of the dynamic fluctuations τ corresponds to the observation time $t_{obs} = 1/\omega = 1/(2\pi f)$ with the attempt frequency ω , and the shortest time τ_0 corresponding to the microscopic flipping time of the fluctuating entities. According to dynamic scaling theory, τ is related to the spin-correlation length, $\tau \propto \xi^z$, and ξ diverges with temperature as $\xi \propto [T_f/(T_f - T_g)]^\nu$ with the dynamic exponent z and the critical exponent ν [49].

The left part of Fig. 5 shows a linear fit of $\ln \tau$ vs $\ln[(T_f - T_g)/T_g]$ allowing values for $z\nu$ and τ_0 to be obtained. These parameters are given in Table III. The $z\nu$ values for Na/K-bir are typical for glassy magnetism [50–52]. Typical values of τ_0 for a canonical SG [52] lie in the range of $\sim 10^{-12}$ – 10^{-14} s; for cluster glasses [26,53,54] with slower dynamics, τ_0 is in the range $\sim 10^{-9}$ – 10^{-11} s. The characteristic relaxation time of our compounds is on the order of $\sim 10^{-12}$ for Na-bir and $\sim 10^{-9}$ for K-bir. These parameters strongly suggest that both compounds exhibit a magnetic cluster glass state.

The dynamic magnetic properties of a glassy system can also be described by the Vogel-Fulcher law [26,55], proposed for magnetically interacting clusters:

$$\tau = \tau^* \times \exp\left[\frac{E_a}{k_B \times (T_f - T_0)}\right]. \quad (4)$$

Here T_0 is a measure of the intercluster interaction strength, and T_0 is known as the Vogel-Fulcher temperature [34,36] and corresponds to the “ideal glass” temperature. Close to T_0 , the Vogel-Fulcher law can be adjusted to match the power law over a large frequency range [52]: $n \frac{40 k_B T_f}{E_a} \sim \frac{25}{z\nu}$. This equation gives $E_a/k_B \sim 28$ K for Na-bir and ~ 18.5 K for K-bir. These values allowed the data to be fitted using Eq. (4) (right-hand panels of Fig. 5), yielding the parameters τ^* , T_0 given in Table III. The extracted τ^* values lie in the range of 10^{-8} – 10^{-13} s anticipated for glassy bulk systems with $\text{Mn}^{3+}/\text{Mn}^{4+}$ magnetic moments [34,59]. For K-bir, the smaller τ^* corresponds to a longer spin-flip time. Our values of T_0 are slightly lower than T_g in the power-law model, as is the case for all SG systems [52]. A similar analysis was reported in the study of Bakaimi *et al.* on $\text{Na}_{0.36}\text{MnO}_2 \cdot 0.2\text{H}_2\text{O}$ [14], but the value of τ^* obtained was unexpectedly large, on the order of 10^{-6} s. The signal from the magnetic impurity phases present in the sample of Ref. [14] might have prevented reliable fitting. In other glassy systems containing mixed-valent $\text{Mn}^{3+}/\text{Mn}^{4+}$, values of τ^* ranging from 10^{-13} to 10^{-9} s have been reported [56–58]. In Eq. (4), T_0 represents a measure of the coupling between the interacting entities [59], where $T_0 \ll E_a/k_B$ corresponds to weak coupling and $T_0 \gg E_a/k_B$ to strong coupling. In the case of Na/K-bir, T_0 is

much smaller than E_a/k_B , which implies the presence of weak interactions between the magnetic clusters.

IV. CONCLUSIONS

In summary, we have synthesized the phase-pure birnessites $\text{Na}_{0.22}\text{MnO}_2 \cdot 0.39\text{H}_2\text{O}$ and $\text{K}_{0.6}\text{MnO}_2 \cdot 0.48\text{H}_2\text{O}$ by the sol-gel method and investigated their magnetic properties. DC magnetic susceptibility measurements show that antiferromagnetic interactions dominate. A bifurcation of the ZFC-FC magnetic susceptibility occurs at low temperatures with a distinct peak in the ZFC branch that suggests the presence of magnetic irreversibility. AC magnetic susceptibility and magnetization decay measurements demonstrate that the magnetic irreversibility likely originates from formation of a cluster glass state below the glass freezing temperature. The position of a peak in the real part of the AC susceptibility, accompanied by a peak in the imaginary component, is frequency dependent and can be described by both the standard critical slowing-down formula and the Vogel-Fulcher law, which confirm the presence of a cluster glass state with weak interactions between clusters at low temperatures.

A comparison of our results with previously reported data on Na-birnessites with different compositions requires us to consider that a higher alkali cation content in the interlayer space leads to a larger proportion of Mn^{3+} cations. This results in an increased likelihood of Jahn-Teller distorted MnO_6 octahedra, as in the case of $\alpha\text{-Na}_{0.9}\text{MnO}_2$ [15,16]. In the opposite situation where there is a large deficiency of alkali cations and a correspondingly larger proportion of Mn^{4+} cations, a larger FM contribution is observed due to Mn^{4+} -O- Mn^{4+} superexchange with a bond angle close to 90° . This is apparent from our magnetization versus applied field measurements where Na-bir exhibits a higher magnetization and wider hysteresis loop compared with K-bir. A larger proportion of Mn^{4+} also suppresses the Jahn-Teller distortion and leads to a Mn^{3+} low-spin state, whereas Mn^{3+} adopts the high-spin state in $\alpha\text{-Na}_{0.9}\text{MnO}_2$ [15,16].

Finally, it should be mentioned that the terms *spin glass* and *cluster glass* encompass a very broad range of specific magnetic states. In many cases, identification of a spin glass/cluster glass is only the beginning of the investigation. For alkali manganites with the birnessite structure, further study of the origin of the magnetic clusters is recommended. Due to the high flexibility in the alkali cation content in the interlayer space of birnessite, it would be interesting to study how to achieve control of the alkali cation occupation and the amount of crystal water, as well as to perform ion exchange of the interlayer species with different alkali cations or other inorganic/organic species. This will open opportunities to tune

TABLE III. Dynamic magnetic properties of Na/K-bir.

Compound	Slowing-down formula		Vogel-Fulcher law		
	τ_0 (s)	$z\nu$	E_a/k_B (K)	τ^* (s)	T_0 (K)
$\text{Na}_{0.22}\text{MnO}_2 \cdot 0.39\text{H}_2\text{O}$	2.6×10^{-12}	13.9	28	4.6×10^{-13}	3.02
$\text{K}_{0.6}\text{MnO}_2 \cdot 0.48\text{H}_2\text{O}$	8.4×10^{-9}	8.7	18.5	4.3×10^{-8}	6.33

the magnetic frustration inherent to birnessites and to create magnetic states.

ACKNOWLEDGMENTS

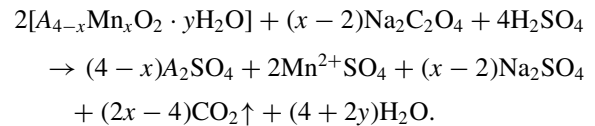
This work was supported by the European Union's Horizon 2020 research and innovation program under Marie Skłodowska-Curie Individual Fellowship, Grant Agreement No. 833550. We would like to thank Dr. Pavan Nukala for assistance with the SEM images and Ing. Jacob Baas for technical advice.

APPENDIX A

Results of the thermal analysis of the samples are presented in Fig. 6. Three main endothermic effects and corresponding mass losses can be identified in the differential scanning calorimetry and thermogravimetric analysis curves in the temperature range 30–500 °C while the samples were heated under a flow of argon gas. The lowest-temperature feature corresponds to surface water evaporation. For Na-bir the mass loss is 5.2% and according to the time derivative of the TG curve (DTG), the loss of water is completed at 95 °C with the maximum of the DSC curve at 84 °C. For K-bir the mass loss is 2.2% and is completed at 79 °C, with the maximum of the DSC curve at 70 °C. The second endothermic effect (maxima in the DSC curve at 115 °C for Na-bir and 127 °C for K-bir) corresponds to the release of interlayer crystal water with mass losses of 7.1% for Na-bir and 7.2% for K-bir. A subsequent, much smaller mass loss of 2.3% for Na-bir and 0.5% for K-bir does not coincide

with an obvious maximum in the DSC curve and might correspond to the release of remaining OH groups in the interlayer space. The last endothermic effect, shown by a broad minimum in the DTG curves and a small mass loss of 1.6% for both compounds (between 351 and 455 °C for Na-bir and 267–411 °C for K-bir) corresponds to a decomposition of the birnessite structure to Mn_2O_3 with the release of oxygen.

The oxidation state of the manganese atoms in the Na/K-bir samples was determined by a back-titration method [60]. Here 0.03 g of Na/K-birnessite was dissolved in 5 mL of 0.5 M aqueous sodium oxalate solution together with 10 mL of 1 M aqueous H_2SO_4 solution. The manganese ions are reduced to Mn^{2+} and the oxalate ions are oxidized to produce CO_2 and H_2O :



Here A is Na^+ or K^+ cations in the birnessite compound, x is the average oxidation state of the Mn ions, and y is the amount of crystal water in the structure.

The unreacted oxalate was then back-titrated with 0.025 M aqueous KMnO_4 solution by the following reaction:

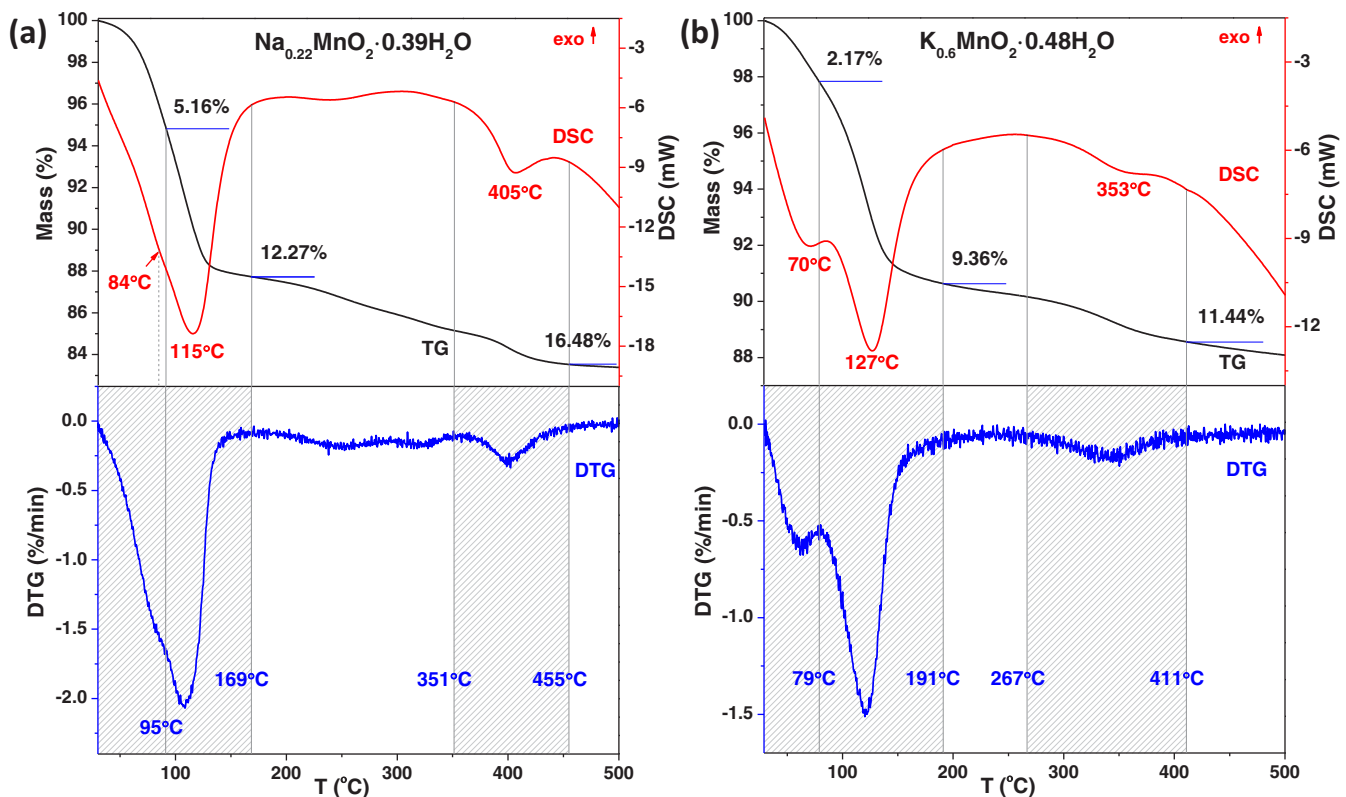
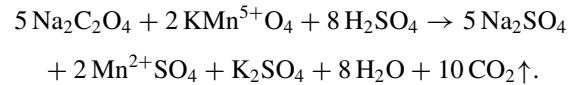


FIG. 6. Thermal analysis of (a) $\text{Na}_{0.22}\text{MnO}_2 \cdot 0.39\text{H}_2\text{O}$, (b) $\text{K}_{0.6}\text{MnO}_2 \cdot 0.48\text{H}_2\text{O}$. The TG and DSC data (top) and the DTG data (bottom) are represented by the black, red, and blue lines respectively.

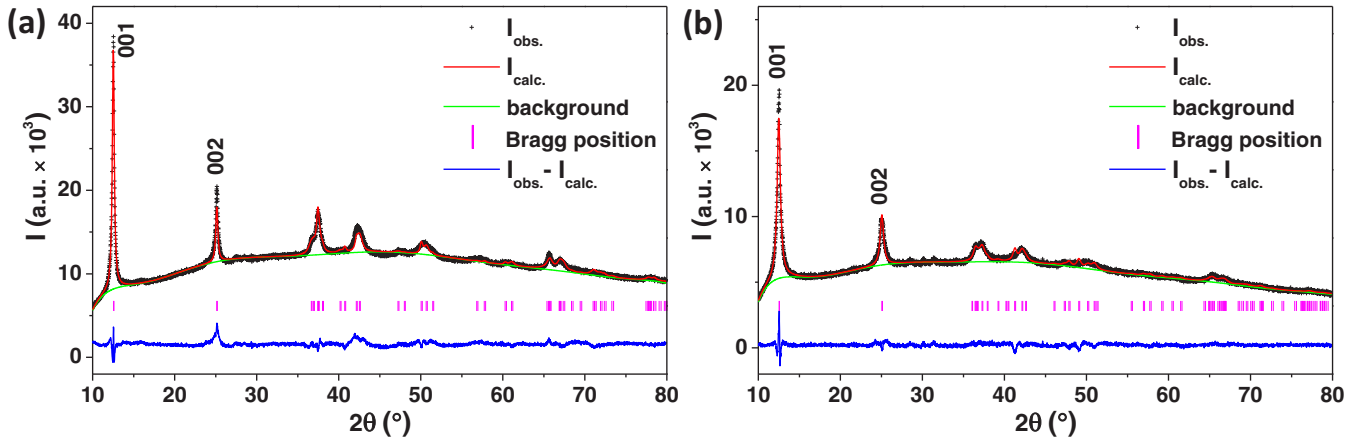


FIG. 7. Rietveld refinements using powder XRD data for (a) $\text{Na}_{0.22}\text{MnO}_2 \cdot 0.39\text{H}_2\text{O}$, (b) $\text{K}_{0.6}\text{MnO}_2 \cdot 0.48\text{H}_2\text{O}$. The observed data are denoted by black crosses, the calculated profile is the red line, and the difference profile is the lower blue line. The pink markers indicate the positions of allowed Bragg peaks.

According to the first chemical reaction the amount of sodium oxalate used to reduce the $\text{Mn}^{3+}/\text{Mn}^{4+}$ in the dissolved birnessite (N_{lox}) corresponds to $N_{\text{lox}} = \frac{x-2}{2} \times N_{\text{bir}}$, where N_{bir} is the amount of used birnessite. Or, that equation can be shown as

$$\frac{m_{\text{bir}}}{[(4-x) \times M_A + M_{\text{Mn}} + 2 \times M_{\text{O}} + y \times M_{\text{H}_2\text{O}}]} = \frac{2}{x-2} \times N_{\text{lox}}.$$

And, the number of moles of unreacted oxalate can thus be determined based on the second reaction, which corresponds to 2.5 times the number of moles of permanganate used.

The values of x and y were obtained by combining the equations above and the equation below for the percentage mass loss of water during heating of the samples (see above):

$$\frac{y \times M_{\text{H}_2\text{O}}}{(4-x) \times M_A + M_{\text{Mn}} + 2 \times M_{\text{O}} + y \times M_{\text{H}_2\text{O}}} = \text{wt } \%_{\text{H}_2\text{O}}.$$

The calculated amount of water is 0.39 molecules per formula unit in the case of Na-bir and 0.48 molecules per formula unit for K-bir. The average manganese oxidation state is +3.78 for Na-bir and +3.37 for K-bir assuming no oxygen or manganese vacancies. This results in a stoichiometry of $\text{Na}_{0.22}\text{MnO}_2 \cdot 0.39\text{H}_2\text{O}$ and $\text{K}_{0.6}\text{MnO}_2 \cdot 0.48\text{H}_2\text{O}$.

APPENDIX B

Figure 7 shows Rietveld fits to the powder XRD data of Na/K-bir. The measured diffractograms show relatively broad peaks, which is common for samples prepared by sol-gel synthesis due to the nanoscale size of the particles formed. In the case of Na-bir, the sample consists of a single phase with the monoclinic structure (space group $C2/m$) previously reported by Post and Veblen [7]. The K-bir sample is also single phase, with peaks that are much broader than for Na-bir. The peak profiles can best be modeled by introducing a triclinic distortion (space group $C\bar{1}$) as reported by Lopano *et al.* [61], which gives clusters of reflections close together.

The fitting was performed using the chemical compositions determined from the thermal analysis and back-titration method (Appendix A). The peak intensities could only be fitted well when a preferential orientation model was included in the fitting, accounting for a preferred packing of crystallites along the [001] direction. In both space groups the Mn^{3+} and Mn^{4+} cations occupy a single position at coordinates (0, 0, 0). Table IV lists the refined Mn–O bond lengths and the Mn–O–Mn bond angles. In the case of Na-bir the bond lengths are consistent with typical values for Mn^{4+} cations, whereas the significantly longer bond lengths in the case of K-bir point to an intermediate valence state of $\text{Mn}^{3+}/\text{Mn}^{4+}$.

Figure 8 shows the structure of $\text{K}_{0.6}\text{MnO}_2 \cdot 0.48\text{H}_2\text{O}$, which is similar to the structure of $\text{Na}_{0.22}\text{MnO}_2 \cdot 0.39\text{H}_2\text{O}$ (Fig. 1). However, for K-bir it was not possible to

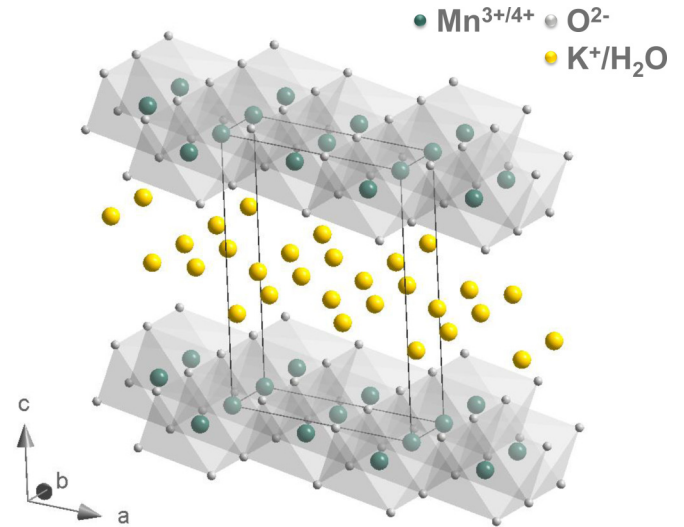


FIG. 8. Schematic representation of the crystal structure of $\text{K}_{0.6}\text{MnO}_2 \cdot 0.48\text{H}_2\text{O}$. The manganese and oxygen atoms are represented by dark green and gray spheres, respectively; the positions of the potassium atoms and H_2O molecules, sharing the same interlayer site, are shown by yellow spheres. One unit cell is indicated by the dark gray lines.

TABLE IV. Refined Mn–O bond lengths and Mn–O–Mn angles in Na/K-bir.

Bond	Length (Å)		Angle	Degree (°)	
	Na _{0.22} MnO ₂ · 0.39H ₂ O	K _{0.6} MnO ₂ · 0.48H ₂ O		Na _{0.22} MnO ₂ · 0.39H ₂ O	K _{0.6} MnO ₂ · 0.48H ₂ O
Mn–O	1.685(9)	1.870(9)	Mn–O–Mn	109.89(29)	97.8(4)
Mn–O	1.685(9)	1.870(9)	Mn–O–Mn	109.89(29)	97.7(4)
Mn–O	1.791(6)	1.982(8)	Mn–O–Mn	105.8(5)	
Mn–O	1.791(6)	1.942(9)			
Mn–O	1.791(6)	1.942(9)			
Mn–O	1.791(6)	1.982(8)			

unambiguously determine the distribution of K⁺ cations and water molecules in the interlayer space. Therefore, the

distribution of K⁺/H₂O was taken to be random in the structural model used in the fitting.

- [1] T. Okubo, S. Chung, and H. Kawamura, *Phys. Rev. Lett.* **108**, 017206 (2012).
- [2] S. Hayami, Sh. Z. Lin, and C. D. Batista, *Phys. Rev. B* **93**, 184413 (2016).
- [3] A. O. Leonov and M. Mostovoy, *Nat. Commun.* **6**, 8275 (2015).
- [4] G. Toulouse, *Commun. Phys.* **2**, 115 (1977).
- [5] J. E. Greedan, *J. Mater. Chem.* **11**, 37 (2001).
- [6] T. Kijima, *Inorganic and Metallic Nanotubular Material. Recent Technologies and Applications, Topics in Applied Physics* (Springer, Berlin, 2010), p. 73.
- [7] J. E. Post and D. R. Veblen, *Am. Mineral.* **75**, 477 (1990).
- [8] V. A. Drits, E. Silvester, A. I. Gorshkov, and A. Manceau, *Am. Mineral.* **82**, 946 (1997).
- [9] K. W. Nam, S. Kim, S. Lee, M. Salama, I. Shterenberg, Y. Gofer, J. Kim, E. Yang, C. S. Park, J. Kim, S. Lee, W. Chang, S. Doo, Y. N. Jo, Y. Jung, D. Aurbach, and J. W. Choi, *Nano Lett.* **15**, 4071 (2015).
- [10] Y. J. Wei, H. Ehrenberg, K. B. Kim, C. W. Park, Z. F. Huang, and C. Baetz, *J. Alloys Compd.* **470**, 273 (2009).
- [11] X. Bie, Y. Wei, L. Liu, K. Nikolowski, H. Ehrenberg, H. Chen, C. Wang, G. Chen, and F. Du, *J. Alloys Compd.* **551**, 37 (2013).
- [12] J. Qu, *J. Environ. Sci.* **20**, 1 (2008).
- [13] H. T. Zhu, J. Luo, H. X. Yang, J. K. Liang, G. H. Rao, J. B. Li, and Z. M. Du, *J. Phys. Chem. C* **112**, 17089 (2008).
- [14] I. Bakaimi, R. Brescia, C. M. Brown, A. A. Tsirlin, M. A. Green, and A. Lappas, *Phys. Rev. B* **93**, 184422 (2016).
- [15] R. L. Dally, R. Chisnell, L. Harriger, Y. Liu, J. W. Lynn, and S. D. Wilson, *Phys. Rev. B* **98**, 144444 (2018).
- [16] R. L. Dally, Y. Zhao, Z. Xu, R. Chisnell, M. B. Stone, J. W. Lynn, L. Balents, and S. D. Wilson, *Nat. Commun.* **9**, 2188 (2018).
- [17] R. J. Clément, D. S. Middlemiss, I. D. Seymour, A. J. Illott, and C. P. Grey, *Chem. Mater.* **28**, 8228 (2016).
- [18] R. Hoppe, G. Brachtel, and M. Jansen, *Z. Anorg. Allg. Chem.* **417**, 1 (1975).
- [19] C. Stock, L. C. Chapon, O. Adamopoulos, A. Lappas, M. Giot, J. W. Taylor, M. A. Green, C. M. Brown, and P. G. Radaelli, *Phys. Rev. Lett.* **103**, 077202 (2009).
- [20] F. Orlandi, E. Aza, I. Bakaimi, K. Kiefer, B. Klemke, A. Zorko, D. Arcon, C. Stock, G. D. Tsibidis, M. A. Green, P. Manuel, and A. Lappas, *Phys. Rev. Mater.* **2**, 074407 (2018).
- [21] S. Ching, E. Welch, S. Hughes, and A. Bahadoor, *Chem. Mater.* **14**, 1292 (2002).
- [22] H. Karaman, R. Barton, B. E. Robertson, and D. Lee, *J. Org. Chem.* **49**, 4509 (1984).
- [23] Q. Feng, L. Liu, and K. Yanagisawa, *J. Mater. Sci. Lett.* **19**, 1567 (2000).
- [24] N. A. Spaldin, *Magnetic Materials Fundamentals and Applications* (Cambridge University Press, Cambridge, 2011).
- [25] N. Marcano, J. C. Gómez Sal, J. I. Espeso, L. Fernández Barquín, and C. Paulsen, *Phys. Rev. B* **76**, 224419 (2007).
- [26] A. Malinowski, V. L. Bezusyy, R. Minikayev, P. Dziawa, Y. Stryanyy, and M. Sawicki, *Phys. Rev. B* **84**, 024409 (2011).
- [27] X.-F. Shen, Y.-S. Ding, J. Liu, Z.-H. Han, J. I. Budnick, W. A. Hines, and S. L. Suib, *J. Am. Chem. Soc.* **127**, 6166 (2005).
- [28] W. J. De Haas and F. K. Du Pré, *Physica* **5**, 501 (1938).
- [29] H. B. G. Casimir and F. K. Du Pré, *Physica* **5**, 507 (1938).
- [30] M. Balanda, *Acta Phys. Pol. A* **124**, 964 (2013).
- [31] S. Körner, A. Weber, J. Hemberger, E.-W. Scheidt, and G. R. Stewart, *J. Low. Temp. Phys.* **121**, 105 (2000).
- [32] X. Zhang, S. Tang, Y. Li, and Y. Du, *Phys. Lett. A* **374**, 2175 (2010).
- [33] B. Aslibeiki, P. Kameli, and H. Salamati, *J. Magn. Magn. Mater.* **324**, 154 (2012).
- [34] J. A. Mydosh, *Spin Glasses: An Experimental Introduction* (Taylor & Francis, London, 1993).
- [35] S. Süllow, G. J. Nieuwenhuys, A. A. Menovsky, J. A. Mydosh, S. A. M. Mentink, T. E. Mason, and W. J. L. Buyers, *Phys. Rev. Lett.* **78**, 354 (1997).
- [36] K. Binder and A. Young, *Rev. Mod. Phys.* **58**, 801 (1986).
- [37] D. L. Stein and C. M. Newman, *Spin Glasses and Complexity* (Princeton University Press, Princeton, 2013).
- [38] L. Néel, *Ann. Geophys.* **5**, 99 (1949).
- [39] W. F. Brown, *Phys. Rev.* **130**, 1677 (1963).
- [40] F. Fernández Barquín, J. C. Gómez Sal, P. Gorria, J. S. Garitaonandia, and J. M. Barandiarán, *Eur. Phys. J. B* **35**, 3 (2003).
- [41] U. Dutta, D. Ghosh, A. Haque, L. Kumar, T. K. Mandal, P. S. Walke, K. Pal, A. Gayen, A. K. Kundu, and M. M. Seikh, *J. Phys.: Condens. Matter* **31**, 225801 (2019).
- [42] S. Pakhira, C. Mazumdar, M. Avdeev, R. N. Bhowmik, and R. Ranganathan, *J. Alloys Compd.* **785**, 72 (2019).

- [43] V. K. Anand, D. T. Adroja, and A. D. Hillier, *Phys. Rev. B* **85**, 014418 (2012).
- [44] C. P. Bean and J. D. Livingston, *J. Appl. Phys.* **30**, S120 (1959).
- [45] J. B. Goodenough, *Phys. Rev.* **117**, 1442 (1960).
- [46] M. Smith, A. Dissanayake, and H. X. Jiang, *Phys. Rev. B* **49**, 4514 (1994).
- [47] W. Kinzel, *Phys. Rev. B* **19**, 4595 (1979).
- [48] P. C. Hohenberg and B. I. Halperin, *Rev. Mod. Phys.* **49**, 435 (1977).
- [49] A. T. Ogielski, *Phys. Rev. B* **32**, 7384 (1985).
- [50] C. Djurberg, P. Svedlindh, P. Nordblad, M. F. Hansen, F. Bodker, and S. Morup, *Phys. Rev. Lett.* **79**, 5154 (1997).
- [51] K. Gunnarsson, P. Svedlindh, P. Nordblad, L. Lundgren, H. Aruga, and A. Ito, *Phys. Rev. Lett.* **61**, 754 (1988).
- [52] J. Souletie and J. L. Tholence, *Phys. Rev. B* **32**, 516 (1985).
- [53] M. D. Mukadam, S. M. Yusuf, P. Sharma, S. K. Kulshreshtha, and G. K. Dey, *Phys. Rev. B* **72**, 174408 (2005).
- [54] R. Mathieu, A. Asamitsu, Y. Kaneko, J. P. He, and Y. Tokura, *Phys. Rev. B* **72**, 014436 (2005).
- [55] J. L. Tholence, *Solid State Commun.* **35**, 113 (1980).
- [56] A. Rostamnejadi, H. Salamati, and P. Kameli, *J. Supercond. Novel Magn.* **25**, 1123 (2012).
- [57] S. Narayana Jammalamadaka, S. S. Rao, J. Vanacken, A. Stesmans, S. V. Bhat, and V. V. Moshchalkov, *AIP Adv.* **1**, 042151 (2011).
- [58] M. H. Ehsani, P. Kameli, M. E. Ghazi, and F. S. Razavi, *Adv. Mater. Res.* **829**, 712 (2014).
- [59] S. Shtrikman and E. P. Wohlfarth, *Phys. Lett. A* **85**, 467 (1981).
- [60] Y. Zhu, X. Liang, H. Zhao, H. Yin, M. Liu, F. Liu, and X. Feng, *Anal. Methods* **9**, 103 (2017).
- [61] C. L. Lopano, P. J. Heaney, J. E. Post, J. Hanson, and S. Komarneni, *Am. Mineral.* **92**, 380 (2007).